Local Advection of Momentum, Heat, and Moisture during the Melt of Patchy Snow Covers

GLEN E. LISTON

Department of Atmospheric Science, Colorado State University, Fort Collins, Colorado

(Manuscript received 7 November 1994, in final form 30 January 1995)

ABSTRACT

A numerical atmospheric boundary layer model, based on higher-order turbulence closure assumptions, is developed and used to simulate the local advection of momentum, heat, and moisture during the melt of patchy snow covers over a 10-km horizontal domain. The coupled model includes solution of the mass continuity equation, the horizontal and vertical momentum equations, an $E-\epsilon$ turbulence model, an energy equation, and a water vapor conservation equation. Atmospheric buoyancy is accounted for, and a land surface energy balance model is implemented at the lower boundary.

Model integrations indicate that advective processes occurring at local scales produce nonlinear horizontal variations in surface fluxes. Under conditions of the numerical experiments, the energy available to melt snow-covered regions has been found to increase by as much as 30% as the area of exposed vegetation increases upwind of the snow cover. The melt increase is found to vary in a largely linear fashion with decreasing snow-covered area for snow-covered areas greater than 25% and in a strongly nonlinear fashion below that value. Decreasing the ratio of patch size to total area, or increasing the patchiness, of the snow cover also leads to nonlinear increases in the energy available to melt the snow. In the limit of a snow cover composed of small patches, melt energy is found to increase linearly as the fractional snow-covered area decreases. In addition, for the purpose of computing grid-average surface fluxes during snowmelt in regional atmospheric models, the results of this study indicate that separate energy balance computations can be performed over the snow-covered and vegetation-covered regions, and the resulting fluxes can be weighted in proportion to the fractional snow cover to allocate the total energy flux partitioning within each surface grid cell.

1. Introduction

The interaction between the atmosphere and the surface below has been shown by numerous studies to strongly influence surface hydrologic processes and climate (Charney et al. 1977; Shukla and Mintz 1982; Sud et al. 1990). Coupled land–atmosphere interaction models commonly assume that the atmospheric surface layer can be treated as horizontally homogeneous over the domain of each model grid cell. In global climate simulations using general circulation models (GCMs), a surface grid cell may typically cover 10^5 km^2. In a regional atmospheric model, a grid cell typically covers an area of 10–100 km^2. In the natural system, the areas covered by these grid elements are clearly inhomogeneous, and these subgrid-scale variations have been shown to significantly influence the surface fluxes of momentum, heat, and moisture (Mahrer and Avissar 1985; Naot and Mahrer 1991; Liston et al. 1993).

In light of the importance of subgrid-scale heterogeneities, attempts have been made to include the effects of spatial variability in land surface parameterizations used within global and regional climate models. One such approach has been to divide each surface grid cell of the model into homogeneous patches. Under the assumption that the horizontal fluxes between the different patches within the cell are much smaller than the vertical fluxes, patches of the same type are lumped into independent homogeneous elements, creating a grid comprised of a collection of these elements (Avissar and Pielke 1989; Koster and Suarez 1992).

From the perspective of a surface energy balance, one dramatic example of landscape heterogeneity in high latitudes is the patchy configurations of vegetation and snow cover present during the snowmelt season. Differences in albedo and roughness length of the two surfaces, in addition to the constraint that the melting snow surface has a temperature of 0°C, contribute to the variations in vertical and horizontal fluxes occurring within the system. Liston (1986) measured the radiative temperatures of snow-free tundra surfaces during snowmelt in Arctic Alaska and found temperatures ranging from 15°C to as high as 42°C for black lichens under conditions of clear skies and low wind speeds. The resulting variations in atmospheric temperature and stability over the snow and vegetation surfaces lead to complex airflow patterns and associated

Corresponding author address: Dr. Glen E. Liston, Department of Atmospheric Science, Colorado State University, Fort Collins, CO 80523.
E-mail: liston@tachu.atmos.colostate.edu

momentum, heat, and moisture fluxes. Additional examples of inhomogeneous landscape configurations include transitions from forests to clearings and land to water bodies, and variations in topography.

The horizontal transport of momentum, heat, and moisture, resulting from landscape heterogeneities, is commonly referred to as local advection. When the relatively warm air lying over snow-free ground is advected over a snow-covered region, an internal boundary layer forms and grows vertically downwind from the leading edge of the snow cover. Further internal boundary layers form and interact as additional vegetation and snow configurations are encountered downwind. As a consequence, large horizontal and vertical gradients develop in the governing atmospheric variables and lead to variations in the associated fluxes.

In this paper, an atmospheric boundary layer model is described and used to study and quantify the local advection of momentum, heat, and moisture during the melt of patchy snow covers. In addition, this work is used to assist in developing strategies for partitioning available energy during snowmelt in regional and global climate models.

2. Model description

The following physically based model has been formulated to describe time-dependent, incompressible, turbulent flows occurring in complex domain configurations. The model is implemented in two dimensions: horizontal and vertical (flow in the second horizontal dimension is considered homogeneous and the Coriolis force is assumed negligible). The turbulence closure scheme used in the model has been formulated to include the processes relevant to complex, heterogeneous boundary layer flows containing regions of high shear and variations in stability. The model is also capable of accounting for complex lower topographic configurations, such as ridges and valleys, although such conditions are not included in this study.

The model is applicable to flow domains ranging from 100 m to several kilometers in the horizontal, and from tens of meters to 1 km in the vertical. This domain corresponds to the large microscale (micro-α) and the small mesoscale (meso-γ) atmospheric processes as defined by Orlanski (1975). As such, the model simulates fields at the subgrid scale of regional (mesoscale) atmospheric models, and also serves as a connecting link between point observations and regional model grid values.

a. General model equations

The turbulent flow field is described by the following continuity, and horizontal and vertical momentum equations:

$$\frac{\partial u}{\partial x} + \frac{\partial w}{\partial z} = 0, \tag{1}$$

$$\frac{\partial u}{\partial t} + u\frac{\partial u}{\partial x} + w\frac{\partial u}{\partial z} = -\frac{1}{\rho}\frac{\partial p}{\partial x} + \frac{\partial}{\partial x}\left(\upsilon_t \frac{\partial u}{\partial x}\right) + \frac{\partial}{\partial z}\left(\upsilon_t \frac{\partial u}{\partial z}\right), \tag{2}$$

$$\frac{\partial w}{\partial t} + u\frac{\partial w}{\partial x} + w\frac{\partial w}{\partial z} = -\frac{1}{\rho}\frac{\partial p}{\partial z} + \frac{\partial}{\partial x}\left(\upsilon_t \frac{\partial w}{\partial x}\right) + \frac{\partial}{\partial z}\left(\upsilon_t \frac{\partial w}{\partial z}\right), \tag{3}$$

where u and w are the velocity components in the x (horizontal) and z (vertical) directions, respectively, p is pressure, t is time, and ρ is the air density. The incompressibility condition employed in the model requires that the depth of the circulations be much less than the scale height of the atmosphere (Pielke 1984). This suggests that the model domain should be confined to the lowest 1 km of the atmosphere.

The turbulent viscosity υ_t is

$$\upsilon_t = c_\mu \frac{E^2}{\epsilon}, \tag{4}$$

where c_μ is an empirical constant (Jones and Launder 1972). The turbulent kinetic energy E and the rate of dissipation of turbulent kinetic energy ϵ are given by

$$\frac{\partial E}{\partial t} + u\frac{\partial E}{\partial x} + w\frac{\partial E}{\partial z} = \frac{\partial}{\partial x}\left(\frac{\upsilon_t}{\sigma_E}\frac{\partial E}{\partial x}\right) + \frac{\partial}{\partial z}\left(\frac{\upsilon_t}{\sigma_E}\frac{\partial E}{\partial z}\right) + S_S + S_B - \epsilon \tag{5}$$

$$\frac{\partial \epsilon}{\partial t} + u\frac{\partial \epsilon}{\partial x} + w\frac{\partial \epsilon}{\partial z} = \frac{\partial}{\partial x}\left(\frac{\upsilon_t}{\sigma_\epsilon}\frac{\partial \epsilon}{\partial x}\right) + \frac{\partial}{\partial z}\left(\frac{\upsilon_t}{\sigma_\epsilon}\frac{\partial \epsilon}{\partial z}\right) + c_{1\epsilon}\frac{\epsilon}{E}(S_S + c_{3\epsilon}S_B) - c_{2\epsilon}\frac{\epsilon^2}{E}, \tag{6}$$

where $c_{1\epsilon}$, $c_{2\epsilon}$, $c_{3\epsilon}$, σ_E, and σ_ϵ are empirical constants (Launder and Spalding 1974; Rodi 1984). The term S_S is a source term resulting from shear,

$$S_S = \upsilon_t\left(\frac{\partial u}{\partial z} - \frac{\partial w}{\partial x}\right)^2, \tag{7}$$

and S_B is a buoyancy source term described by

$$S_B = g_z \frac{\upsilon_t}{\sigma_t}\frac{1}{\theta}\frac{\partial \theta}{\partial z}, \tag{8}$$

where g_z is the gravitational acceleration in the z direction, σ_t is the turbulent Prandtl number, and θ is the potential temperature.

The energy conservation equation that describes the evolution of potential temperature θ is

$$\frac{\partial \theta}{\partial t} + u\frac{\partial \theta}{\partial x} + w\frac{\partial \theta}{\partial z} = \frac{\partial}{\partial x}\left(\Gamma_t \frac{\partial \theta}{\partial x}\right) + \frac{\partial}{\partial z}\left(\Gamma_t \frac{\partial \theta}{\partial z}\right), \quad (9)$$

where Γ_t is the turbulent diffusivity for heat. The conservation equation for the vapor phase specific humidity, or mass of water vapor per unit mass of air q_v, is

$$\frac{\partial q_v}{\partial t} + u\frac{\partial q_v}{\partial x} + w\frac{\partial q_v}{\partial z} = \frac{\partial}{\partial x}\left(\Gamma_t \frac{\partial q_v}{\partial x}\right) + \frac{\partial}{\partial z}\left(\Gamma_t \frac{\partial q_v}{\partial z}\right), \quad (10)$$

where the turbulent diffusivity for mass and heat have been assumed equal.

The turbulent Prandtl number is given by the ratio of the turbulent viscosity ν_t to the turbulent diffusivity Γ_t,

$$\sigma_t = \frac{\nu_t}{\Gamma_t}, \quad (11)$$

and is assumed to take the form adopted by Bartzis et al. (1991),

$$\sigma_t = \begin{cases} \mathrm{Pr}\,\dfrac{(1 - 9\ \mathrm{Ri})^{-1/2}}{(1 - 15\ \mathrm{Ri})^{-1/4}}, & \mathrm{Ri} < 0 \\ \mathrm{Pr}, & \mathrm{Ri} \geq 0, \end{cases} \quad (12)$$

where the molecular Prandtl number $\mathrm{Pr} = \mu\, c_p/\lambda$, μ is the molecular viscosity, c_p is the specific heat of air at constant pressure, and λ is the thermal conductivity. The Richardson number Ri is given by

$$\mathrm{Ri} = -\frac{g_z}{\theta}\frac{\partial \theta/\partial z}{(\partial u/\partial z)^2}. \quad (13)$$

The empirical constants used in the model are considered generally universal and are assumed to be (ASCE 1988; Liston et al. 1993) $c_\mu = 0.03$, $c_{1\epsilon} = 1.16$, $c_{2\epsilon} = 1.92$, $\sigma_E = 1.0$, $\sigma_\epsilon = 1.3$, and

$$c_{3\epsilon} = \begin{cases} 1, & S_B > 0 \\ 0, & S_B \leq 0. \end{cases} \quad (14)$$

If the incompressibility assumption was relaxed, then the potential temperature θ would be related to the actual temperature T and the specific humidity q_v through the virtual temperature (Pielke 1984). Consistent with the incompressibility assumption, the difference between the potential and actual temperature has been assumed negligible. For the case of neutrally buoyant conditions, the above model has been found to successfully simulate separated atmospheric surface layer flows (Liston et al. 1993).

b. Boundary conditions

The incoming velocity profile is assumed to be

$$u = \frac{u_*}{\kappa}\ln\left(\frac{z}{z_0}\right), \quad (15)$$

where u_* is the shear velocity, κ is von Kármán's constant, and z_0 is the roughness height. This logarithmic profile is also used as a lower boundary condition for the horizontal velocity and to set the horizontal velocity at the upper boundary. The incoming and lower surface vertical velocities are set to zero. Incoming profiles of E and ϵ are given by

$$E = \frac{u_*^2}{c_\mu^{1/2}} \quad (16)$$

(Frost et al. 1975) and

$$\epsilon = \frac{u_*^3}{\kappa z} \quad (17)$$

(Panofsky and Dutton 1984), respectively, and are also used as lower boundary conditions for these variables.

The inflow boundary conditions for potential temperature and specific humidity are obtained from meteorological station observations of air temperature and relative humidity or vapor pressure. Confining the region of the inflow boundary to adiabatic transformations leads to a potential temperature that is constant with height and, in this study, is assumed to be equal to the observed air temperature T_r at reference height z_r. The specific humidity q_{vr} at the reference height is given by computing the vapor pressure e_r according to

$$e_r = 10^{(11.40 - 2353/T_r)}\mathrm{RH}, \quad (18)$$

where RH is the observed relative humidity (expressed as a fraction) and

$$q_{vr} = 0.622\frac{e_r}{p_r}, \quad (19)$$

where a representative atmospheric pressure p_r for the location of interest is given by

$$p_r = p_0 \exp\left(-\frac{Z_g}{H}\right), \quad (20)$$

where p_0 is a reference sea level pressure (101 300 Pa), H is the scale height of the atmosphere ($\approx$8000 m), and Z_g is the elevation of the study site (Wallace and Hobbs 1977).

The inflow specific humidity profile is obtained from

$$q_v = q_{vr} - \frac{E_v}{\kappa u_* \rho}\ln\left(\frac{z}{z_r}\right), \quad (21)$$

where E_v is the evaporation rate (Brutsaert and Kustas 1985) determined from the surface latent heat flux Q_e according to

$$E_v = -\frac{Q_e}{L_v}, \quad (22)$$

where L_v is the latent heat of vaporization.

At the lower boundary, the surface temperature boundary condition is computed by implementing a

complete surface energy balance, as described in the next section. The vapor pressure at the lower boundary is

$$e_0 = 10^{(11.40-2353/T_0)}\beta, \quad (23)$$

where T_0 is the surface temperature and β is the soil moisture fraction (0–1) obtained from a soil hydrology model; in this study, β is set equal to 1, under the assumption that during snowmelt there is an abundance of moisture available. Thus, the specific humidity at the surface can be obtained by substituting e_0 into Eq. (19).

The outflow boundary condition for u, the upper and outflow boundary conditions for w, E, ϵ, θ, and q_v, and the conditions at all boundaries for p are defined to be

$$\frac{\partial \Omega}{\partial n} = 0, \quad (24)$$

where Ω is the dependent variable of interest, and n is oriented normal to the boundary.

Initial conditions for model integrations are obtained by distributing the inflow boundary conditions throughout the flow domain. The integrations then proceed until an equilibrium state is obtained during the period of interest.

c. *Surface energy balance*

To determine the surface-temperature boundary condition, a complete energy balance is computed at the surface. The surface energy balance equation is

$$(1 - \alpha_s)Q_{si} + Q_{li} + Q_{le} + Q_h + Q_e + Q_c = Q_m, \quad (25)$$

where Q_{si} is the solar radiation reaching the surface of the earth, Q_{li} is the incoming longwave radiation, Q_{le} is the emitted longwave radiation, Q_h is the turbulent exchange of sensible heat, Q_e is the turbulent exchange of latent heat, Q_c is the conductive energy transport, Q_m is the energy flux available for melt, and α_s is the albedo of the surface. Energy transports toward the surface are defined to be positive.

The solar radiation striking a horizontal surface Q_{si} is given by

$$Q_{si} = S^*\Upsilon \sin\omega, \quad (26)$$

where S^* is the solar irradiance at the top of the atmosphere striking a surface normal to the solar beam ($=1370$ W m^{-2}) (Kyle et al. 1985), and Υ is the net sky transmissivity, or the fraction of solar radiation that makes it to the surface. The solar elevation angle ω is defined to be

$$\sin\omega = \sin\delta \sin\phi + \cos\delta \cos\phi \cos\tau, \quad (27)$$

where ϕ is latitude, τ is the hour angle measured from local solar noon, and δ is the solar declination angle approximated by

$$\delta = \phi_T \cos\left[2\pi\left(\frac{d - d_r}{d_y}\right)\right], \quad (28)$$

where ϕ_T is the latitude of the tropic of Cancer (23.45°N), d is the Gregorian day, d_r is the day of the summer solstice (173), and d_y is the average number of days in a year (365.25).

To account for the scattering, absorption, and reflection of shortwave radiation by clouds, the solar radiation is scaled according to

$$\Upsilon = (0.6 - 0.2 \sin\omega)(1.0 - 0.5\sigma_c), \quad (29)$$

where σ_c represents the fraction of cloud cover (Burridge and Gadd 1974).

An analytical downward longwave radiation equation that considers clear skies and standard atmospheric conditions has been developed by Brutsaert (1975). To correct apparent deficiencies in this formulation at air temperatures below 0°C (Aase and Idso 1978), Satterlund (1979) suggested the empirical description

$$Q_{li} = 1.08\{1 - \exp[-(0.01 e_r)^{T_r/2016}]\}\sigma T_r^4, \quad (30)$$

where the atmospheric vapor pressure e_r (Pa) is given by Eq. (18). In the current study, no attempt has been made to modify this formulation for Q_{li} to account for the presence of clouds.

The longwave radiation emitted by the snow surface is computed under the assumption that snow emits as a graybody

$$Q_{le} = -\varepsilon_s \sigma T_0^4, \quad (31)$$

where T_0 is the snow surface temperature, σ is the Stefan–Boltzmann constant, and ε_s is the surface emissivity, assumed to be 0.98.

The turbulent exchange of sensible and latent heat, Q_h and Q_e, respectively, are given by (Price and Dunne 1976)

$$Q_h = \rho c_p D_h \zeta (T_r - T_0) \quad (32)$$

$$Q_e = \rho L_v D_e \zeta \left(0.622 \frac{e_r - e_0}{p_r}\right), \quad (33)$$

where ζ is a nondimensional stability function. The terms D_h and D_e are exchange coefficients for sensible and latent heat, respectively,

$$D_{h,e} = \frac{\kappa^2 u_r}{[\ln(z_r/z_0)]^2}, \quad (34)$$

where u_r is the wind speed at reference height z_r. The stability function ζ is defined following the surface flux parameterization of Louis (1979). Under unstable atmospheric conditions (Ri < 0), ζ modifies the turbulent fluxes through the formula

$$\zeta = 1 - \frac{\eta \,\mathrm{Ri}}{1 + \gamma |\mathrm{Ri}|^{1/2}}, \quad (35)$$

where $\eta = 9.4$ and

$$\gamma = \varphi\eta \frac{D_{h,e}}{u_r}\left(\frac{z_r}{z_0}\right)^{1/2}, \quad (36)$$

where $\varphi = 5.3$. Under stable atmospheric conditions ($\mathrm{Ri} > 0$),

$$\zeta = (1 + \eta^* \mathrm{Ri})^{-2}, \quad (37)$$

where $\eta^* = \eta/2$.

Heat conduction flux at the surface is

$$Q_c = -k_g \left.\frac{dT_g}{dz}\right|_0, \quad (38)$$

where T_g is the ground temperature and k_g is the effective thermal conductivity of the vegetation–soil matrix. In this study, the conductive flux is assumed to be negligible.

To solve the system of equations for the surface temperature, the equations are cast in the form $f(T_0) = 0$ and solved iteratively for T_0 using the Newton–Raphson method. In the presence of snow, surface temperatures $T_0 > 0$°C, resulting from the surface energy balance, indicate that energy is available for melting Q_m. The amount of energy available is then computed by setting the surface temperature to 0°C and recomputing the surface energy balance. A similar procedure is adopted to compute the energy available to freeze Q_f any liquid water that may be present.

d. Numerical solution procedure

Equations (1)–(14), in conjunction with the boundary conditions found in Eqs. (15)–(38), comprise the coupled, nonlinear system of equations that models the unsteady, two-dimensional turbulent velocity, temperature, and specific humidity fields. The SIMPLER (semi-implicit method for pressure-linked equations, revised) finite control volume algorithm described by Patankar (1980) is used to solve the system of partial differential transport equations.

3. Computational results

In what follows, the preceding planetary boundary layer model is used to describe land–atmosphere interactions during the melt of patchy snow covers. The simulations consider conditions typical of snow melt in Arctic Alaska, and the computations focus on melt conditions occurring during solar noon. The domain of interest covers a horizontal distance of 10 km and a vertical height of 1 km. There are 200 horizontal grid cells with a spacing of 50 m. In the vertical, there are 40 levels, which start at a spacing of 0.05 m at the ground and are stretched by a factor of 1.23 to reach a spacing of 160 m at the top of the domain.

The model has been used to simulate conditions over a wide range of snow–vegetation patterns (Fig. 1).

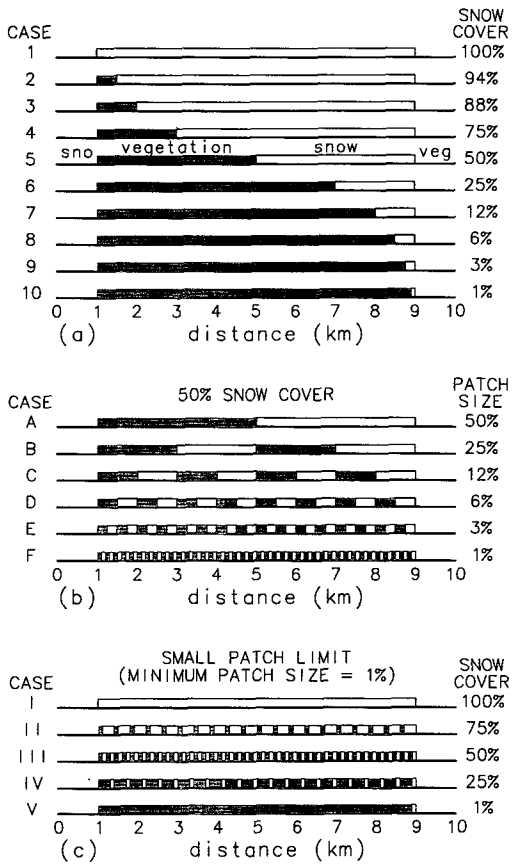

FIG. 1. Snow–vegetation patterns used in model integrations.

Cases 1–10 represent a gradual increase in the size of the vegetation cover upwind of the snow patch of interest. As such, these cases correspond to a decrease in snow-covered area within the domain, with snow cover ranging from 100% to 1.25%. Cases A–F represent the condition of 50% snow cover, where the size of the snow patches making up the snow cover varies from 100 m to 4 km. Cases I–V represent a combination of cases 1–10 and A–F, where the snow-covered fraction is composed of evenly distributed, small snow patches of 100-m minimum size (1.25% of 8-km domain). This small patch limit is expected to represent the case of a well-mixed atmosphere. All of the snow–vegetation patterns used in this study include a 1-km snow coverage at the inflow boundary (left-hand side of Fig. 1), and a 1-km segment of exposed vegetation at the outflow boundary (right-hand side of Fig. 1). Cases 1 and I, 5 and A, 10 and V, and F and III are identical.

In the simulations, the difference between snow and vegetation is defined through the roughness length and the albedo. The roughness length of snow is assumed to equal 0.001 m, and that of the vegetation (tundra) is 0.035 m. The temperature of the melting snow surface is 0°C, with an albedo of 0.5. The albedo of the vegetation is defined to be 0.15. The energy balance

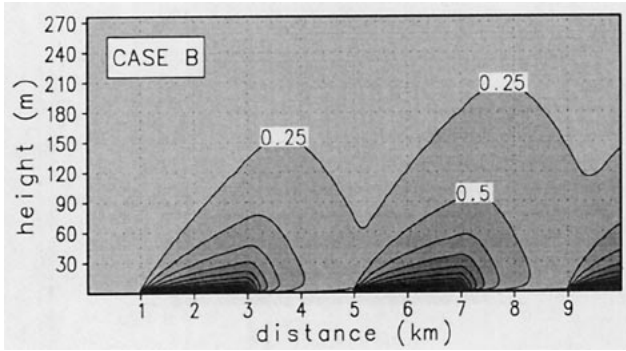

FIG. 2. Model-simulated air temperature (°C) field for case B, with inflow reference height wind speed of 2 m s^{-1}. Contour interval is 0.25°C.

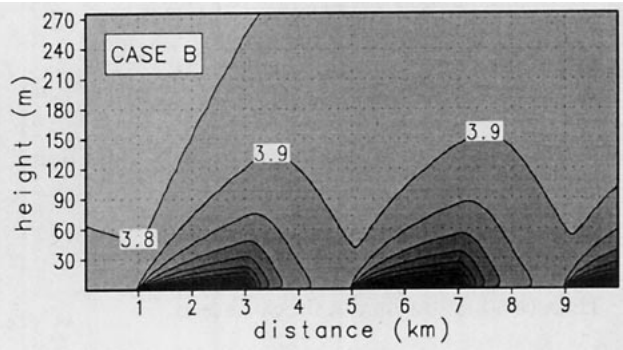

FIG. 3. Model-simulated specific humidity (g kg^{-1}) field for case B, with inflow reference height wind speed of 2 m s^{-1}. Contour interval is 0.1 g kg^{-1}.

computations are performed for the following case: the latitude is 68°N, the time is during solar noon on 15 May, and the sky is cloud-free. The reference-height temperature and relative humidity at the upwind boundary are defined to be 0°C and 97%, respectively. These upwind temperature and relative humidity conditions were chosen such that the surface and the atmosphere were in equilibrium. At the upwind boundary, the 2-m horizontal wind velocity varies from 1 to 16 m s^{-1}, and the vertical wind velocity is defined to be zero. These conditions represent an extreme case from the perspective of snowmelt; on 15 May the solar radiation is near its peak, and incoming solar radiation is reduced during other times of the day and under other cloud scenarios. Snowmelt from below and from the snow patch edges inward, is considered negligible, and is not included in the simulations.

Figure 2 displays the air temperature field (°C) for case B, at a wind speed of 2 m s^{-1}. Wind flow is from left to right. The heat islands produced by the exposed vegetation are evident, as are the merging temperature contours downwind of the vegetation. These heat plumes are transported downwind and produce higher air temperatures over the snow-covered areas. These air temperatures, over snow, decrease with downwind distance from the leading edge of each snow patch, and they increase with the number of upwind vegetation elements. Figure 3 shows the computed specific humidity field (g kg^{-1}) for case B with a 2 m s^{-1} wind speed. The presence of the vegetation–snow patterns strongly influence the local atmospheric water vapor distribution. Simulations of the other vegetation–snow patterns (Fig. 1) produce similar qualitative results for both temperature and specific humidity.

The surface energy balance differs widely for the vegetation and snow-covered areas. Results of the energy balance computations for case 5 (case A), with an 8 m s^{-1} reference level wind speed, are found in Fig. 4 (energy flux toward the surface is defined to be positive). The net solar radiative flux at the surface Q_{ns} [$Q_{ns} = (1 - \alpha_s)Q_{si}$] differs in response to the different albedos of snow and vegetation. Incoming longwave radiation Q_{li} follows the air temperature and is continuous over the vegetation–snow boundaries. The negative of the emitted longwave radiation $-Q_{le}$ follows the surface temperature. It is constant over the melting snow and discontinuous at the vegetation–snow boundaries. These radiative energy fluxes are similar to those measured by Hinzman (1990) during snow melt in Arctic Alaska.

Under the conditions of this simulation, the negatives of the sensible heat flux $-Q_h$ and latent heat flux $-Q_e$ are generally minimal over snow (Fig. 4), but they reach a maximum at the leading edge of the snow cover, and they decrease in a very nonlinear fashion as the distance downwind from the leading snow edge increases. Over the vegetation portion of the domain, these terms are positive, much larger, and roughly constant, with values of approximately 240 W m^{-2} for both $-Q_h$ and $-Q_e$. The energy available to melt snow Q_m is only computed over the snow-covered regions, and

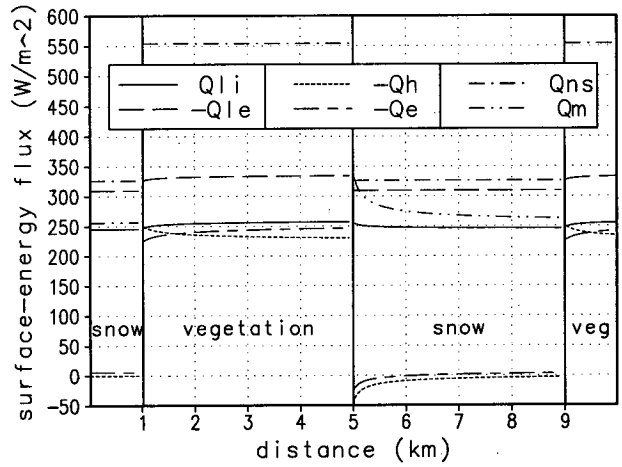

FIG. 4. Model-simulated surface energy balance components for case 5 (case A), with inflow reference height wind speed of 8 m s^{-1}.

it decreases with distance from the leading edge of the snow patch. Over the snow, the incoming and emitted longwave fluxes balance to within approximately 60 W m^{-2}, and the snow melt is seen to be dominated by the available net solar radiation. The nonlinear increase in melt at the leading edge of the snow cover occurs in response to increases in sensible and latent heat fluxes in that region.

The horizontal variability of melting energy, for the 8 m s^{-1} runs, for each of cases 1–10 and A, B, C, and E are plotted in Figs. 5a and 5b, respectively. The melting energy over each snow patch was nondimensionalized by subtracting the melt energy at the inflow snow patch, dividing the result by the same inflow melt energy, and expressing the final value as a percent. The length and locations of these curves correspond to the snow-covered area for each case. Cases 1, D, and F have been left out for clarity. If plotted, case 1 would form a straight line, of value equal to 0%, across the domain. These figures show the enhanced melt energy resulting from the local advection of momentum, heat, and moisture. Consider, for example, case 5 (case A), Fig. 5a. At the leading edge of the snow patch, the melting energy is 29% higher than that present at the inflow snow patch. This increase in energy decreases to 3% at the trailing edge of the snow cover in response to the presence of the lower-temperature snow surface. The other cases are qualitatively similar.

Integration of the curves in Figs. 5a and 5b, to obtain averages over the snow-covered part of the flow domain, allows a quantitative analysis of the effect that local advection, snow-patch size, and fractional snow-covered area have on snow melt. Figure 6a illustrates the increase in melt energy as the snow-covered area reduces from 100% to 1.25% (cases 1–10). Figure 6b describes the increase in melt energy as the ratio of snow-patch size to total area decreases from 50% to 1.25% (or patch size goes from 4 km to 100 m), for the case of 50% snow cover (cases A–F). The dependence of these curves on wind speed is also illustrated and found to level off at around 8 m s^{-1}. The simulations show these snow-cover and snowmelt relationships to be largely linear for snow-covered areas greater than 25%, and for patch size to total area ratios greater than 12%. For values smaller than these limits, this linearity breaks down. In addition, these figures indicate that in the computation of the energy available to melt the snow, both the total fractional snow cover and the

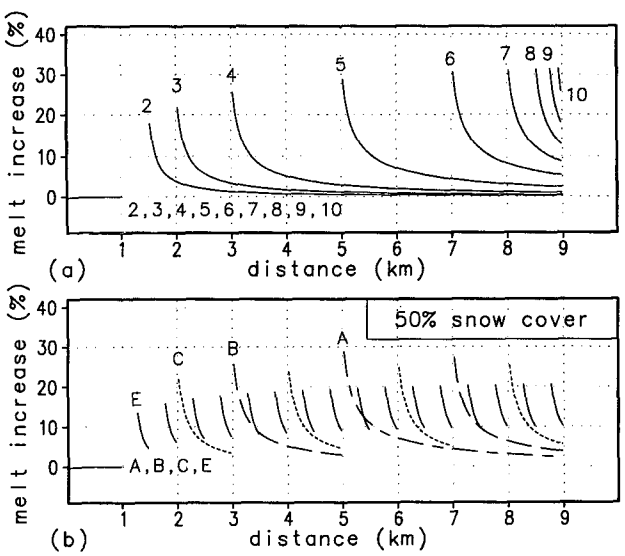

FIG. 5. Horizontal variability of melt across the snow patches, (a) cases 1–10, and (b) cases A, B, C, and E. (Cases D and F not shown for the sake of clarity.) The increase in snowmelt energy has been nondimensionalized by the melt energy at the inflow snow patch. The inflow reference height wind speed is 8 m s^{-1}.

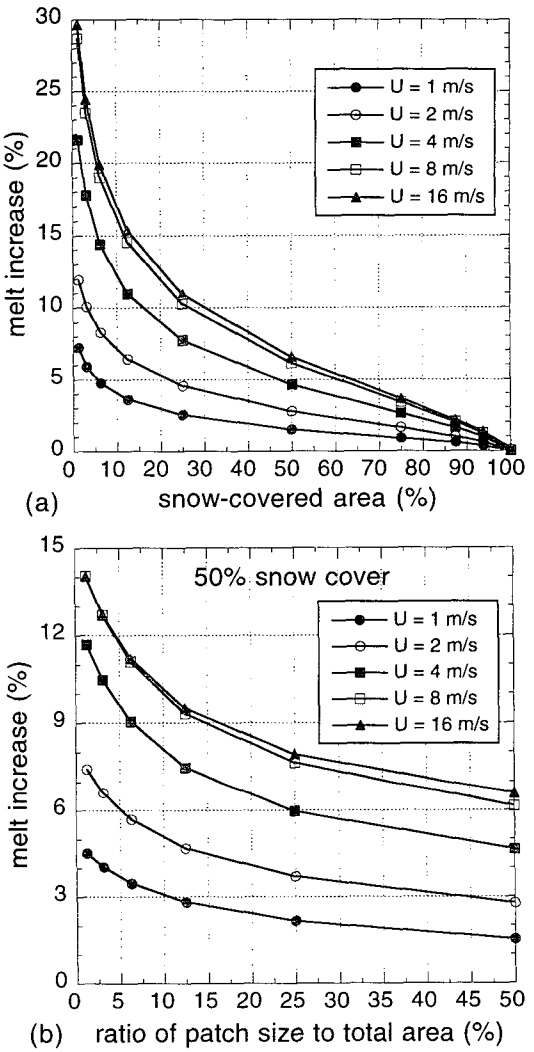

FIG. 6. Average melt energy computed from profiles in Fig. 5: (a) the effect of fractional snow-covered area on melt energy (cases 1–10), and (b) the effect of snow-patch size on melt energy for the condition of 50% snow cover (cases A–F).

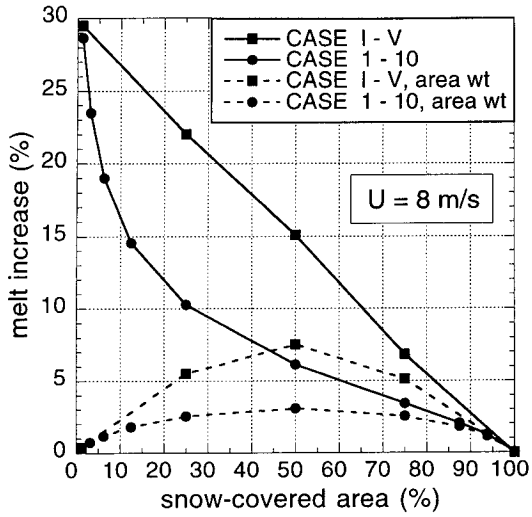

FIG. 7. Melt-energy variation with snow-covered area for cases I–V, the small snow-patch size limit. Also shown are cases 1–10 from Fig. 6a and the two curves when weighted by snow-covered area. Inflow reference height wind speed is 8 m s^{-1}.

distribution of the snow cover across the domain, or the patchiness, are important features.

The melt-energy variation with snow-covered area for cases I–V, the small snow-patch size limit, is given in Fig. 7 for the conditions of an inflow reference-height wind speed of 8 m s^{-1}. These simulations represent the combined influence of cases 1–10 and A–F and are indicative of the case of a well-mixed atmosphere. Under such conditions, the increase in available energy to melt snow is expected to increase linearly with net radiation and, consequently, to be proportional to the fractional area of exposed vegetation (i.e., 1—fractional snow-covered area). The 8 m s^{-1} curve from Fig. 6a (cases 1–10) is also included for reference. Choosing minimum snow-patch sizes greater than 100 m produces curves that lie within the region enclosed by these two curves. These two curves can be area weighted by the snow-covered fractional area, and the result is also shown in Fig. 7 (dashed lines). Since the nonlinearity in melt occurs when the snow-covered area is approaching zero, the grid-averaged influence of the enhanced melt is suppressed.

In Fig. 7, to ensure capturing the effects of the 100-m snow and vegetation patches, the simulations for cases I–V were performed using a 10-m grid in the horizontal direction (for a total of 1000 grid cells in the x direction) instead of the 50-m grid used in the integration of cases 1–10. As a result of this increase in resolution, the two simulations (solid lines) in Fig. 7 produce melt values that differ by 0.8% for the identical snow configurations of cases 10 and V (1.25% snow cover). Simulations of the other snow–vegetation configurations indicate that running the simulations with this increase in resolution was justified only for the case of small ($\leq$100 m) snow patches.

Figure 8 displays the results of integrating the surface fluxes (see Fig. 4) over the snow-covered (Fig. 8a) and the vegetation-covered (Fig. 8b) regions of the domain for cases 1–10. Over the snow-covered areas, the incoming longwave radiation, melt energy, and sensible and latent heat are nonlinear as the fractional snow cover varies. The net solar radiation is constant and equal to 326 W m^{-2} over the snow (not shown in Fig. 8a). In these simulations, the increase in melt energy closely parallels, and is largely the consequence of, increased incoming longwave radiation resulting from the advection of heat from the upwind vegetation patches (see Fig. 2), combined with enhanced sensible and latent heat fluxes near the leading edge of the snow cover. The nonlinearity is essentially confined to the conditions of snow-covered area less than 25%. Over the vegetation-covered regions, the incoming and

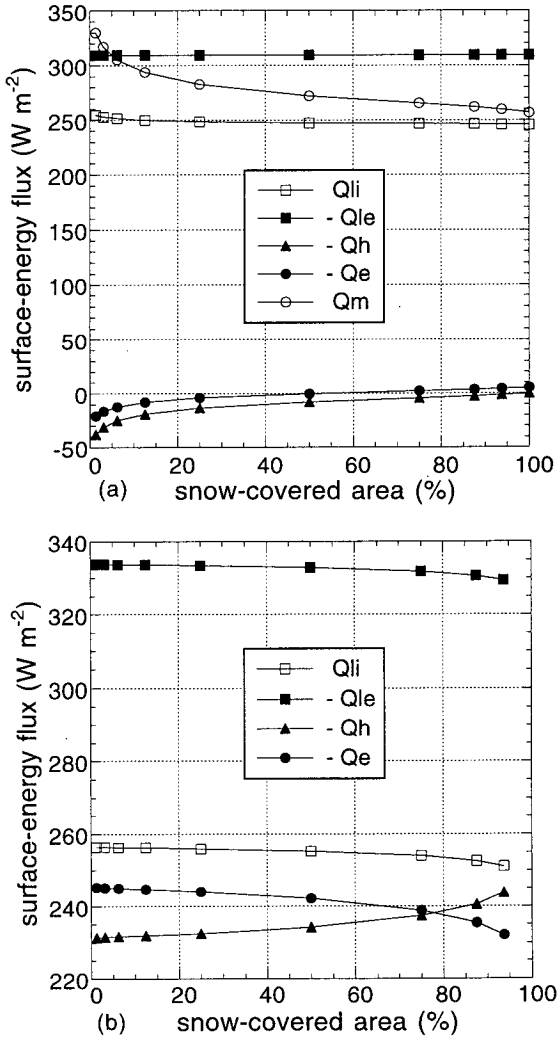

FIG. 8. Average surface energy flux dependence on snow-covered area for cases 1–10: (a) over snow and (b) over vegetation. Inflow reference height wind speed is 8 m s^{-1}.

emitted longwave radiation and the sensible and latent heat are nonlinear with snow-covered area. This nonlinearity is present under fractional snow-covered areas greater than 75%. In addition, the sensible and latent heat fluxes over vegetation largely dominate those found over snow. The net solar radiation over the vegetation is constant and equal to 554 W m^{-2} (not shown in Fig. 8b).

The results of integrating the surface fluxes over the entire domain (combining both snow and vegetated regions, Fig. 8) for cases 1–10 are given in Fig. 9. In addition to the expected linear increase in net solar radiation as snow-covered area decreases, the other energy balance components display strong linear relationships to fractional snow cover (close inspection reveals that these distributions are not perfectly linear). Weighting the curves in Figs. 8a and 8b, by the fractional snow cover and fractional vegetation cover, respectively, shows that when the nonlinearities are most prevalent, the associated surface type covers the least area. Consequently, the relationships represented in Fig. 9 are found to be largely linear. A similar plot for cases I–V is nearly identical to Fig. 9, with the greatest variation being an 11 W m^{-2} increase in melt energy for the 50% snow-covered area.

The implication derived from Fig. 9, that the components of the surface energy balance vary linearly with snow-covered area, leads to the conjecture of simple schemes for partitioning the available solar radiative energy into the other surface fluxes. As an example, the surface energy flux distributions in Fig. 9 can be closely reproduced by computing a surface energy balance for the case of 100% snow cover and one for the case of 0% snow cover, and then applying an areal weighting that is identical to the fractional snow and vegetation cover. The results of this computation are found in Fig. 10 (solid lines). Also included, for reference, are the values from Fig. 9 (dashed lines).

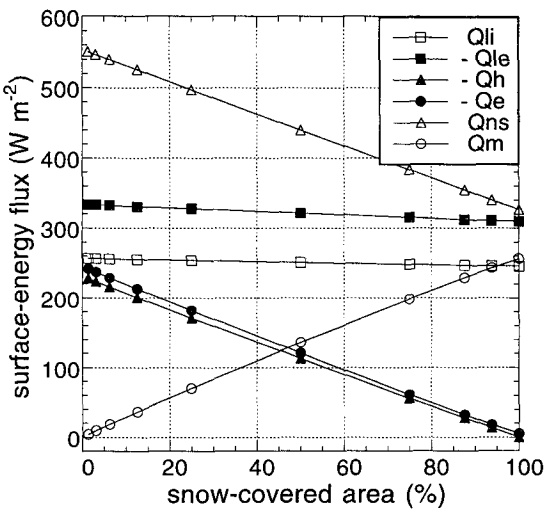

FIG. 9. Average surface energy fluxes over the entire domain (combining both snow and vegetated regions, Fig. 8) for cases 1–10.

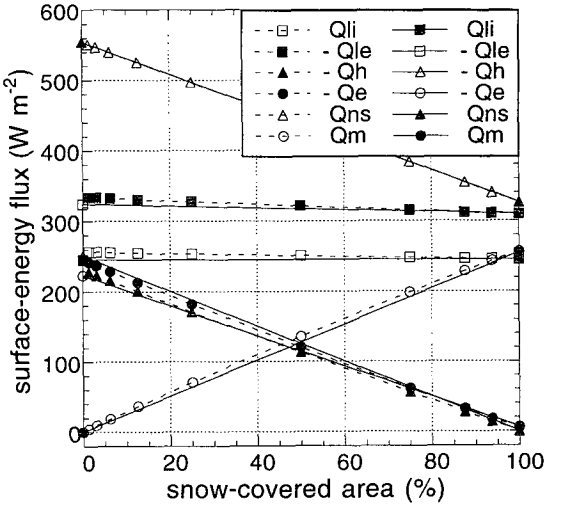

FIG. 10. Energy balance components resulting from areal weighting the energy balance over snow and the energy balance over vegetation (solid lines), in the absence of any local advection influences. Also shown is the energy balance resulting from the full computations presented in Fig. 9 (dashed lines).

Further model integrations suggest that the linearity found in Fig. 10 is not sensitive to variations of the incoming temperature and humidity boundary conditions. This is because of the dramatic difference in net solar, sensible, and latent heat fluxes between snow-covered and vegetative-covered surfaces. Changes in the upwind boundary conditions do influence the magnitude of the sensible and latent heat fluxes, but the linearity and the appropriateness of linear weighting the flux computed over snow and that computed over vegetation is still appropriate.

The preceding simulations have clarified two features of land–atmosphere interactions during the melt of patchy snow covers: first, the role of local advection on the enhancement of snow melt has been quantified, and the energy available to melt snow-covered regions has been found to increase dramatically (by as much as 30%) as the area of exposed vegetation increases upwind of the snow cover, and second, for the purposes of partitioning available solar radiative energy into grid-average surface fluxes under conditions of fractional snow cover, it may be appropriate to apply linear weightings, determined by the fractional snow-covered area, to the surface fluxes computed or known under conditions of complete snow cover and complete vegetation cover.

4. Discussion and conclusions

Regional and global atmospheric models generally resolve grid-average surface fields of wind speed, air

temperature, vapor pressure, and surface fluxes; the details of any subgrid-scale flow features are generally unaccounted for. This leads to the question of the role that local advection plays in modifying the surface fluxes at subgrid scales. An atmospheric boundary layer model has been developed and used to study the local advection of momentum, heat, and moisture during snow melt. The degree to which local advection influences snowmelt will be a function of several factors, including wind speed, surface roughness, and albedo, cloud cover, and vapor pressure. The influence of local advection on modifying the surface energy balance during midday melting is seen in the variations of energy fluxes over the snow-covered and the vegetation-covered areas of Fig. 4. The variations are most significant at the leading edges of the vegetation and snow-cover patches, and are much less dramatic than the differences between the average fluxes computed over the individual covers of snow and vegetation. Numerous investigators have noted this dramatic increase of net radiation, when the snow surface is replaced by tundra, during snowmelt in the Arctic (e.g., Weller and Holmgren 1974; Hinzman 1990).

From the perspective of the snow on the ground, the influences of local advection of heat and moisture on the melt of downwind snow covers are significant and dependent upon both area of upwind exposed vegetation and size of the patches comprising the snow cover (Figs. 6 and 7). The melt increase is found to vary linearly for snow-covered areas greater than 25%, and in a nonlinear fashion below that value. Decreasing the ratio of patch size to total area, or increasing the patchiness, of the snow cover also leads to increases in the energy available to melt the snow. These processes are found to increase with wind speed, up to around 8 m s^{-1}, where an asymptote is reached.

From the perspective of the atmosphere, and its interaction with larger-scale (-8 km) land surface fluxes, local advection-related contributions to snow melt are found to be of secondary importance, giving way to the more predominant radiation-related contributions. For the purposes of computing grid-average surface fluxes during snowmelt in regional atmospheric models, the results of this study indicate that each regional-model surface grid cell can be divided into homogeneous subdomains of snow and vegetation. In addition, all of the snow patches within each regional model grid cell can be lumped together to form one large snow-covered region, leading to a simple measure of the areal fraction of snow and vegetation within each grid cell. Separate energy balance computations can be performed over the snow-covered and vegetation-covered regions, and the resulting fluxes can be weighted in proportion to the fractional snow cover to allocate the total energy-flux partitioning within each surface grid cell.

Such linear relationships between snow–vegetation–atmosphere interactions have significant implications for the development of land surface parameterizations for use in regional and global atmospheric models. In addition, these findings lend support to the approaches of Avissar and Pielke (1989) in their regional modeling, and Koster and Suarez (1992) in their general circulation modeling; they divide each model grid into subgrid areas composed of several separate vegetation types, permanent ice cover, and open water. The findings of the current study suggest that a similar accounting for the fractional snow-covered area will assist in providing a realistic partitioning of surface fluxes under conditions of patchy snow covers.

The conclusions reached in this investigation have been based on a limited number of simulations. In addition, a more complex model might produce slightly different quantitative results, but the quality of the model and the integrations performed in this study are expected to be sufficient to reach the presented conclusions. Variations in snowmelt rates of natural snow covers arise from variations in solar radiation resulting form slope, shading, etc., features that are not included in the model. The inclusion of a full diurnal cycle in the integrations is expected to reduce the effects illustrated here for the case of snow melt during solar noon. Also, the influences of large-scale advective processes have not been considered and might modify the conclusions reached herein. In addition, further simulations are necessary to establish the influences of other landscape heterogeneities such as transitions from forests to clearings, soil moisture variations, and topographic diversity.

Beyond indicating the appropriateness of linearly aggregating regional atmospheric model subgrid-scale surface fluxes during snowmelt, this study has highlighted the need to quantify the fractional snow-covered area during the evolution of seasonal snow covers. Such a description of snow areal extent is expected to result primarily from data collected by airborne and satellite sensors, but would also benefit from the combined input of meteorological data, ground-based snow observations, digital elevation data, and forest canopy datasets. Realistically incorporating snow cover in regional atmospheric models and GCMs is expected to improve the subsequent analysis and simulation of land–atmosphere interactions, weather, and climate.

Acknowledgments. The author wishes to thank Drs. Max Suarez, Randy Koster, Dorothy Hall, and Al Chang of NASA/Goddard Space Flight Center for their comments and support during this modeling effort.

REFERENCES

Aase, J. K., and S. B. Idso, 1978: A comparison of two formula types for calculating long-wave radiation from the atmosphere. *Water Resour. Res.*, **14**, 623–625.

ASCE, 1988: Turbulence modeling of surface water flow and transport: Part IV. *J. Hyd. Engr.*, **114**, 1034–1051.

Avissar, R., and R. A. Pielke, 1989: A parameterization of heterogeneous land surfaces for atmospheric numerical models and

its impact on regional meteorology. *Mon. Wea. Rev.*, **117,** 2113–2136.

Bartzis, J. G., A. G. Venetsanos, M. Varvayanni, N. Catsaros, and A. Megaritou, 1991: ADREA-I: A three-dimensional transient transport code for complex terrain and other applications. *Nucl. Tech.*, **94,** 135–148.

Brutsaert, W., 1975: On a derivable formula for long-wave radiation from clear skies. *Water Resour. Res.*, **11,** 742–744.

——, and W. P. Kustas, 1985: Evaporation and humidity for neutral conditions over rugged hilly terrain. *J. Climate Appl. Meteor.*, **24,** 915–923.

Burridge, D. M., and A. J. Gadd, 1974: The Meteorological Office operational 10 level numerical weather prediction model (December 1974). British Meteorological Office Tech. Notes 12 and 48, 57 pp.

Charney, J. G., W. J. Quirk, S. H. Chow, and J. Kornfield, 1977: A comparative study of the effects of albedo change on drought in semi-arid regions. *J. Atmos. Sci.*, **34,** 1366–1385.

Frost, W., W. L. Harper, and G. H. Fichtl, 1975: Analysis of atmospheric flow over a surface protrusion using the turbulence kinetic energy equation. *Bound.-Layer Meteor.*, **8,** 401–417.

Hinzman, D. L., 1990: The interdependence of the thermal and hydrological processes of an arctic watershed and their response to climatic change. Ph.D. dissertation, University of Alaska, Fairbanks, 403 pp.

Jones, W. P., and B. E. Launder, 1972: The prediction of laminarization with a two-equation model of turbulence. *Int. J. Heat Mass Transfer,* **15,** 301–314.

Koster, R. D., and M. J. Suarez, 1992: Modeling the land surface boundary in climate models as a composite of independent vegetation stands. *J. Geophys. Res.*, **97**(D3), 2697–2715.

Kyle, H. L., P. E. Ardanuy, and E. J. Hurley, 1985: The status of the *Nimbus-7* earth-radiation-budget data set. *Bull. Amer. Meteor. Soc.*, **66,** 1378–1388.

Launder, B. E., and D. B. Spalding, 1974: The numerical computation of turbulent flow. *Comput. Methods Appl. Mech. Eng.*, **3,** 269–289.

Liston, G. E., 1986: Seasonal snowcover of the foothills region of Alaska's arctic slope: A survey of properties and processes. M.S. thesis, University of Alaska, Fairbanks, 123 pp.

——, R. L. Brown, and J. Dent, 1993: Application of the E-ϵ turbulence closure model to separated atmospheric surface-layer flows. *Bound.-Layer Meteor.*, **66,** 281–301.

Louis, J.-F., 1979: A parametric model of vertical eddy fluxes in the atmosphere. *Bound.-Layer Meteor.*, **17,** 187–202.

Mahrer, Y., and R. Avissar, 1985: A numerical study of the effects of soil surface shape upon the soil temperature and moisture regimes. *Soil Sci.*, **139,** 483–490.

Naot, O., and Y. Mahrer, 1991: Two-dimensional microclimate distribution within and above a crop canopy in an arid environment: Modeling and observational studies. *Bound.-Layer Meteor.*, **56,** 223–244.

Orlanski, I., 1975: A rational subdivision of scales for atmospheric processes. *Bull. Amer. Meteor. Soc.*, **56,** 527–530.

Panofsky, H. A., and J. A. Dutton, 1984: *Atmospheric Turbulence.* John Wiley and Sons, 397 pp.

Patankar, S. V., 1980: *Numerical Heat Transfer and Fluid Flow.* Hemisphere Publishing, 197 pp.

Pielke, R. A., 1984: *Mesoscale Meteorological Modeling.* Academic Press, 612 pp.

Price, A. G., and T. Dunne, 1976: Energy balance computations of snowmelt in a subarctic area. *Water Resour. Res.*, **12,** 686–694.

Rodi, W., 1984: *Turbulence Models and Their Application in Hydraulics.* Int. Assoc. Hydraulic Res., 104 pp.

Satterlund, D. R., 1979: An improved equation for estimating long-wave radiation from the atmosphere. *Water Resour. Res.*, **15,** 1649–1650.

Shukla, J., and Y. Mintz, 1982: The influence of land-surface evapotranspiration on earth's climate. *Science,* **215,** 1498–1501.

Sud, Y. C., P. J. Sellers, Y. Mintz, M. D. Chow, G. K. Walker, and W. E. Smith, 1990: Influence of the biosphere on the global circulation and hydrologic cycle—A GCM simulation experiment. *Agric. For. Meteor.*, **52,** 133–180.

Wallace, J. M., and P. V. Hobbs, 1977: *Atmospheric Science, An Introductory Survey.* Academic Press, 467 pp.

Weller, G., and B. Holmgren, 1974: The microclimates of the arctic tundra. *J. Appl. Meteor.*, **13,** 854–862.